Material influence in newly proposed ferroelectric energy harvesters

Dan Wang[1] (iD)**, Roderick Melnik[2] and Linxiang Wang[1]**

Abstract

Recently, a novel method for mechanical energy harvesting has been proposed, which is based on stress-induced polarization switching in ferroelectric materials. Compared with the traditional piezoelectric energy harvesters, a huge improvement in the output energy has already been theoretically demonstrated. In this article, the influence of different materials on the energy-harvesting performance associated with this new strategy is further studied. The state-of-the-art phase-field model is adopted to investigate the nonlinear hysteretic energy-harvesting process in two nanoscale ferroelectric energy harvesters, which are respectively based on two typical ferroelectric materials—single-crystal $BaTiO_3$ and $PbTiO_3$. In both cases, the effects of the bias voltage and bias resistance are carefully investigated and the optimum values are obtained. Later, the energy-harvesting process and energy flow details in both harvesters working at the optimum conditions are presented and carefully compared in the context of real applications. Furthermore, the energy-harvesting performance of a $BaTiO_3$-based nanoscale piezoelectric energy harvester with equivalent material size is additionally simulated with the finite element method and compared with the corresponding results of the ferroelectric energy harvesters, where obvious advantages associated with the new strategy are demonstrated.

Keywords

Ferroelectric energy harvester, material influence, phase field, energy flow

Introduction

In the past two decades, mechanical energy harvesting has emerged as a promising method to power wireless sensor networks and implantable biomedical devices, generating great interest from researchers around the world (Karami and Inman, 2012; Priya and Inman, 2009; Shaikh and Zeadally, 2016). Generally, there are three principal ways to convert the ambient mechanical energy into useful electricity: electromagnetic, electrostatic, and piezoelectric effects (Invernizzi et al., 2016; Roundy et al., 2003). Among these three traditional methods, piezoelectric energy harvester (PEH) is the one that has been investigated most intensively due to its large electro-mechanical coupling coefficient. The idea of using piezoelectric effect for energy harvesting has already been extended to the nanoscale region (Wang and Song, 2006). Nanoscale PEHs or piezoelectric nanogenerators with different one-dimensional (1D) nanostructures, such as nanowires and nanobelts, are of great interest in energy harvesting for flexible or wearable electronics due to their supreme mechanical properties (Chen et al., 2017; Nafari et al., 2017). However, the energy density harvested via piezoelectric effect is still not sufficient, especially for applications in

low-frequency mechanical environments. Different methods have been proposed in the literature to improve the energy-harvesting performance, including but not limited to, designing different mechanical structures to lower the natural frequency of the systems to meet the frequency range of the mechanical sources (Rezaeisaray et al., 2015; Sharpes et al., 2015; Zhou et al., 2017), introducing nonlinear effects into the energy-harvesting structures to broaden the resonance frequency range (Daqaq et al., 2014; Yang and Zu, 2016a), trying different energy-harvesting management circuits to optimize the output energy (Lefeuvre et al., 2017; Shen et al., 2010), and employing materials with better properties (Ren et al., 2010; Yang and Zu, 2016b). In addition to the efforts associated with these

[1]State Key Laboratory of Fluid Power and Mechatronic Systems, Zhejiang University, Hangzhou, China
[2]MS2Dicovery Interdisciplinary Research Institute, Wilfrid Laurier University, Waterloo, ON, Canada

Corresponding author:
Linxiang Wang, State Key Laboratory of Fluid Power and Mechatronic Systems, Zhejiang University, No.38, Zheda Road, Hangzhou 310027, China.
Email: wanglx236@zju.edu.cn

traditional methods, innovative mechanism-based strategies have also been proposed, for example, diverse electrochemical harvesters (Kim et al., 2016, 2017), harvesters using the coupling between flowing fluids and electronic charges (Liu et al., 2007; Yin et al., 2014), and the triboelectric nanogenerators (Fan et al., 2012; Wu et al., 2017; Zi et al., 2016).

Recently, a new method for mechanical energy harvesting has been proposed, which is based on stress-induced polarization switching phenomena in ferroelectric materials (Balakrishna and Huber, 2016; Wang et al., 2017). Different from the traditional piezoelectric mechanical energy harvesting, which is confined to the linear piezoelectric region, a non-180° ferroelastic polarization switching is induced in this new method to seek more polarization variations. The huge polarization changes associated with stress-induced polarization switching process result in a great improvement of the output energy. The energy density, which is several orders of magnitude higher than its counterpart harvested by traditional linear piezoelectric effect, has been theoretically demonstrated. By introducing a bias electric field, the robustness deficiency problem associated with the original prototype has been successfully tackled (Wang et al., 2017). Due to its great potential in real applications and the complicated nonlinear hysteretic phenomena involved, this new method requires a more detailed analysis.

In this article, the influence of different materials on the energy-harvesting performance is under investigation. Differences between two single-crystal $BaTiO_3$- and $PbTiO_3$-based nanoscale ferroelectric energy harvesters (FEHs) are demonstrated and discussed. As in our previous work (Wang et al., 2017), the state-of-the-art phase-field model is numerically implemented to carefully investigate the energy-harvesting performance. Before the phase-field study, the energy flow chart of this newly proposed FEH is established for the first time, which enhances the understanding of the basic working mechanism of this new strategy. Based on the energy flow chart, two different energy-harvesting efficiencies are defined, which serve as two important figures of merit when accessing the performance of the energy harvesters. In the phase-field simulation, the input stain amplitudes in these two FEHs are carefully designed to ensure that the ferroelastic polarization switching can be induced. In addition, values of the bias voltage and bias resistance are optimized to obtain the best energy-harvesting performance in both cases. Later, details about the energy-harvesting process and energy flow in the FEHs working at the optimum conditions are illustrated and discussed in the context of real applications. Finally, the energy-harvesting performance of a $BaTiO_3$-based nanoscal PEH with equivalent material size is additionally simulated and compared with the results of the new strategy, where huge advantages associated with the newly proposed FEHs are demonstrated.

Basic working mechanism and energy flow chart of FEH

Before the phase-field investigation of the material influence, the basic working mechanism of the newly proposed FEH is briefly reviewed. As a subgroup of piezoelectric materials, ferroelectric materials are distinguished for their spontaneous polarizations under Curie temperature, which can be switched by external stress. A macroscopic polarization variation, which is much larger than that with piezoelectric effect and can be used for mechanical energy harvesting, is associated with the stress-induced polarization switching process. For details regarding polarization switching phenomena in ferroelectric materials, Shu and Bhattacharya's (2001) work can be referred to. It is noticed that, in the literature, the terminology "ferroelectric" is always confused with "piezoelectric," and FEH/PEH are both used to describe energy harvesting via linear piezoelectric effect indiscriminatingly. To make a distinction, in this article, FEH is specified for energy harvesting via stress-induced polarization switching, which is a typical feature of ferroelectric materials. A schematic representation of a base-excited single degree of freedom ferroelectric energy-harvesting system is shown in Figure 1. Compared with linear PEH, the main difference lies in the energy transducer element. The piezoelectric transducer is replaced by a ferroelectric transducer. Input stress/strain from the mechanical part induces a polarization switching process in the transducer. With appropriate electrodes and energy-harvesting circuit arrangement, the huge macroscopic polarization variation associated with stress-induced polarization switching leads to a large electric current in the output circuit. In this way, the mechanical energy is converted into the electricity. In Figure 1, the mass-spring-damper system is a simple representation of the mechanical part. In real applications, nonlinear distributed mechanical structures, such as different types of cantilevers, can be employed. The energy-harvesting circuit is the simple one adopted in our previous work (Wang et al., 2017), where the DC voltage source provides a bias electric field to impose a preferred orientation for polarization switching, and the resistance serves as the energy-harvesting element. Considering the similarity between this newly proposed FEH and traditional PEH, hints and references can be obtained from so many achievements regarding PEH, which gives the biggest advantage over other new mechanism-based energy-harvesting methods.
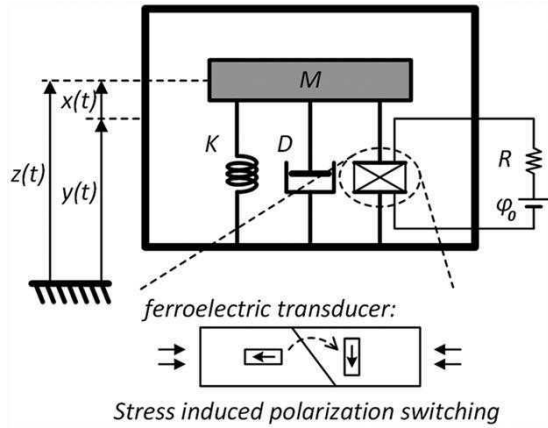
**Figure 1.** Schematic representation of a base-excited single degree of freedom FEH.

In addition to the basic working mechanism reviewed above, the energy flow chart of FEH is established for the first time in this section. The details are illustrated in Figure 2. Compared with the energy flow chart of PEH (Liang and Liao, 2012), the energy flow within the mechanical part is identical, while distinctions exist for the energy flows within the transducer part and electrical part. As polarization switching process is inherently a dissipative process, part of the input energy to the ferroelectric transducer is dissipated and finally converted to the thermal energy, which is represented by the energy flow g in Figure 2. In contrast, in traditional PEH, the dissipated energy within the transducer part is very small and can be omitted. Besides, in the energy flow chart of PEH, the input mechanical energy is directly converted to electrical energy and the inverse electrical energy is directly converted to mechanical energy via the piezoelectric transducer. However, it is not the case in FEH.

Instead, part of the input energy is stored in the transducer and an inner loop is formed in the energy flow chart. As shown in the following section, this energy is stored in the ferroelectric materials in the form of Landau energy, elastic energy, electric energy, coupling energy, and gradient energy. For the electrical part, an electrical energy flow o provided by the bias voltage source is added in the energy flow chart for FEH. As discussed in our previous work (Wang et al., 2017), the amount of this energy is related to the current leakage effect of the ferroelectric materials. If this leakage effect can be omitted, the net amount of the electrical energy flow o in a complete cycle reduces to zero. It is also noticed that in Liang and Liao's (2012) work, there is no inner loop associated with the electrical part, which is not a valid assumption if there are any energy storage elements, such as capacitance or inductance, existing in the energy-harvesting circuits.

To assess the performance of an energy-harvesting system, two kinds of figures of merit are very important. One is the net amount of output energy density and the other is the system efficiency. Here, based on the energy flow chart established above, two energy-harvesting efficiencies are proposed. One is the total energy conversion efficiency, which can be expressed as

$$\eta_T = \frac{E_m}{E_a - E_w} \tag{1}$$

where E_a, E_m, and E_w, respectively denote the energy contained in the energy flow a, m, and w as in Figure 2. η_T is related to the capability of the system to convert the mechanical energy to the electrical one. On the other hand, the effective energy-harvesting efficiency, which can be expressed as
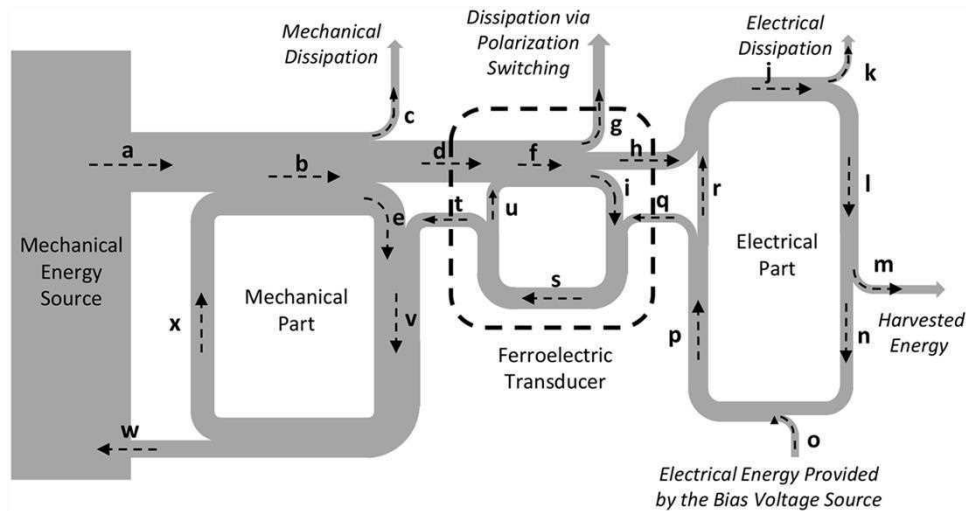
Figure 2. Illustration of the energy flow chart of FEH.

$$\eta_E = \frac{E_m}{E_a} \qquad (2)$$

captures the ability of the system to harvest the electrical energy from a fixed amount of input mechanical energy. These two efficiencies are both very important in analyzing and trying to optimize the system performance and will be adopted in the following section to access the material influence.

Phase-field investigation of the material influence

Phase-field model and numerical implementation details

Phase-field model is a sort of diffusive interface model, which can simulate the microstructures and track the domain wall motions in ferroelectrics in a straightforward and robust way (Chen, 2002; Su and Landis, 2007; Zhang and Bhattacharya, 2005). Phase-field model for ferroelectrics has already been employed by different researchers to investigate the properties of ferroelectric-based nanoscale devices (Balakrishna and Huber, 2016; Balakrishna et al., 2014; Lich et al., 2015, 2017; Wang et al., 2018). As in our previous work, the state-of-the-art phase-field model is adopted in this article to investigate the nonlinear hysteretic polarization switching phenomena involved in the energy-harvesting process. The specific model adopted in this work is deduced as a gradient flow of the total free energy of the material. In the following, the model details are briefly reviewed. The total free energy of a single-crystal ferroelectric material can be expressed as (Zhang and Bhattacharya, 2005)

$$
\begin{aligned}
F = {}& \frac{a_1}{2}\left(P_1^2 + P_2^2\right) + \frac{a_2}{4}\left(P_1^4 + P_2^4\right) + \frac{a_3}{2}P_1^2 P_2^2 \\
& + \frac{a_4}{6}\left(P_1^6 + P_2^6\right) + a_5\left(P_1^4 P_2^2 + P_1^2 P_2^4\right) \\
& - \frac{b_1}{2}\left(\varepsilon_{11}P_1^2 + \varepsilon_{22}P_2^2\right) - \frac{b_2}{2}\left(\varepsilon_{11}P_2^2 + \varepsilon_{22}P_1^2\right) \\
& - b_3(\varepsilon_{12} + \varepsilon_{21})P_1 P_2 \\
& + \frac{c_1}{2}\left(\varepsilon_{11}^2 + \varepsilon_{22}^2\right) + c_2\varepsilon_{11}\varepsilon_{22} + \frac{c_3}{2}\left(\varepsilon_{12}^2 + \varepsilon_{21}^2\right) \\
& + \frac{g}{2}\left(P_{1,1}^2 + P_{1,2}^2 + P_{2,1}^2 + P_{2,2}^2\right)
\end{aligned}
\qquad (3)
$$

where $a_1 - a_5$, $b_1 - b_3$, $c_1 - c_3$, and g are material-specific parameters; P_i denotes the Cartesian components of the polarization vector; ε_{ij} is the components of the strain tensor; and $P_{i,j}$ is the components of the polarization gradient. The first five terms in equation (3) are the Landau free energy; the following three terms denote the coupling energy; the terms in the fifth line are the elastic energy, and the last term represents the gradient energy. By choosing the polarization P_i as the order parameter and employing the gradient flow

method, the governing equation for the order parameter can be obtained as (Zhang and Bhattacharya, 2005)

$$\mu\dot{P}_i = \left(\frac{\partial F}{\partial P_{i,j}}\right)_{,j} - \frac{\partial F}{\partial P_i} - \varphi_{,i} \qquad (4)$$

where $1/\mu > 0$ captures the mobility of the domain wall, and φ is the electric potential. In ferroelectrics, equation (4) is also called the time-dependent Ginzburg–Landau (TDGL) equation. For the model completeness, the TDGL equation needs to be solved together with the elastic and electrical governing equations

$$\sigma_{ji,j} = 0 \qquad (5)$$
$$D_{i,i} = 0 \qquad (6)$$

where $\sigma_{ij} = \partial F/\partial \varepsilon_{ij}$ is the Cartesian components of the stress tensor, and $D_i = P_i - \kappa_0\varphi_{,i}$ is the components of the electric displacement vector. Equations (4) to (6) altogether constitute the governing equations of the phase-field model, which can well characterize the behavior of the ferroelectric transducer in FEH.

In the following, the phase-field model reviewed above is numerically implemented to investigate the material influence on the performance of the FEHs. As a demonstration, two nanoscale FEHs, which are respectively based on single-crystal $BaTiO_3$ and $PbTiO_3$, are considered. To fully capture the dynamics of the entire energy-harvesting system and optimize the system performance, the phase-field model, that is, equations (4) to (6), should be coupled with models for the mechanical part and the energy-harvesting circuit. However, when attached to a macroscopic mechanical structure, the back force from the nanoscale ferroelectric transducer is very small and can be omitted. For simplicity, the coupling effect with respect to the mechanical part is not considered in this investigation, and a given strain signal is directly fed into the phase-field model to mimic the mechanical input. On the other hand, the coupling, with respect to the harvesting circuit, is incorporated into the phase-field model through an appropriate accommodation of the electrical boundary conditions as in our previous work (Wang et al., 2017). Periodic boundary conditions are applied on the left and right boundaries. More detailed information regarding the boundary conditions is listed in Table 1. The computational area for each transducer material is 160 nm × 40 nm as illustrated in Figure 3. Details of the model parameters for the two FEHs considered in this work are listed in Table 2. Finite element method with backward time differentiation strategy is adopted to solve the model, which is numerically implemented in COMOSOL Multiphysics. Note that domain walls in phase-field model are diffusive, and their width defines a characteristic length scale (Su and Landis, 2007)
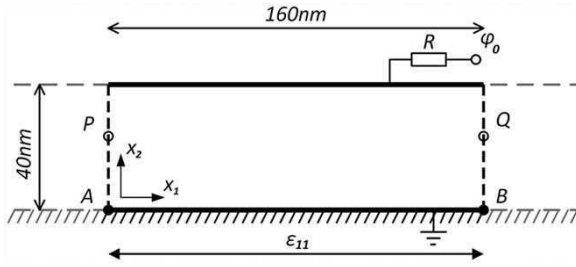
Figure 3. Illustration of the computational area for the phase-field simulation.

$$l_0 = \sqrt{\frac{g \cdot P_0}{E_0}} \qquad (7)$$

where P_0 is the spontaneous polarization, and E_0 is the electric field value required to induce homogeneous 180° polarization switching. With the parameters listed in Table 2, the specific values for $BaTiO_3$ and $PbTiO_3$ are 1.28 nm and 1.14 nm, respectively. Consequently, square meshes with element size equal to 1 nm are employed in both simulations, in which case, domain walls span across several elements, and sufficient simulation accuracy is guaranteed.

Optimization of the bias voltage and bias resistance

As discussed in our previous work (Wang et al., 2017), the bias voltage and bias resistance values have big impacts on the energy-harvesting performance of the FEHs. In this subsection, the phase-field simulations are first employed to optimize the bias voltage and bias resistance values in these two nanoscale FEHs. To induce the non-180° polarization switching in the energy-harvesting process, the amplitudes of the input strains need to be carefully designed. With some thermodynamic calculations, several important material-specific constants are provided in Table 3, which would be helpful in the following discussions. Based on these calculated material properties, the exact form of the input strain signals in both harvesters adopted in the simulations is given as

$$\varepsilon_{11}(t) = \frac{1.2\left(\varepsilon_{11}^0 - \varepsilon_{22}^0\right)}{2} \cos\left(\frac{2\pi t}{T}\right) + \frac{1.2\left(\varepsilon_{11}^0 + \varepsilon_{22}^0\right)}{2} \qquad (8)$$

Table 1. Boundary conditions for the phase-field simulations.

	Left and right boundary	Lower boundary	Upper boundary
Elastic equation	$u_1\|_Q - u_1\|_B = u_1\|_P - u_1\|_A$ $u_2\|_Q - u_2\|_B = u_2\|_P - u_2\|_A$	$u_1 = \varepsilon_{11}(t) \cdot x_1$ $u_2 = 0$	$\sigma_{12} = 0$ $\sigma_{22} = 0$
Electrical equation	$\varphi\|_Q = \varphi\|_P$	$\varphi = 0$	$\varphi = R \cdot \frac{d \int D_2 dx_1}{dt} + \varphi_0$ [a]
TDGL equation	$P_1\|_Q = P_1\|_P$ $P_2\|_Q = P_2\|_P$	$P_{1,2} = 0$ $P_{2,2} = 0$	$P_{1,2} = 0$ $P_{2,2} = 0$

TGDL: time-dependent Ginzburg–Landau.
[a]The dynamic effect of the energy-harvesting circuit is incorporated into the current model through this boundary condition.

Table 2. Material parameters for the phase-field simulations (Units: SI).

|	a_1	a_2	a_3	a_4	a_5	g [a]
$BaTiO_3$	−5.61e7	7.70e8	3.02e7	3.96e10	2.90e9	1.00−10
$PbTiO_3$	−3.45e8	1.69e9	1.47e9	1.56e9	6.10e8	2.77e−10
	b_1	b_2	b_3	c_1	c_2	c_3
$BaTiO_3$	2.59e10	−1.94e9	3.19e9	1.35e11	4.38e10	5.41e10
$PbTiO_3$	2.24e10	5.02e8	3.75e9	1.39e11	4.33e10	5.56e10

[a]The parameter g is important in determining the domain wall thickness and domain wall surface energy. The specific value for $BaTiO_3$ is taken from Su and Landis' work (2007) and the value for $PbTiO_3$ is from Lich et al.'s (2015) work. For other material parameters, Pertsev et al.'s (1998) work is referred to.

Table 3. Several important material-specific constants.

	P_0	E_0	ε_{11}^0	ε_{22}^0
$BaTiO_3$	0.26 C/m^2	15.828 MV/m	0.0081	−0.0032
$PbTiO_3$	0.757 C/m^2	161.19 MV/m	0.051	−0.0149
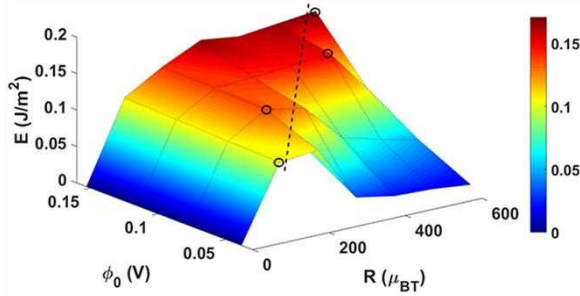
Figure 4. Demonstration of the influence of the bias voltage and bias resistance on the output energy density in BaTiO$_3$-based FEH.
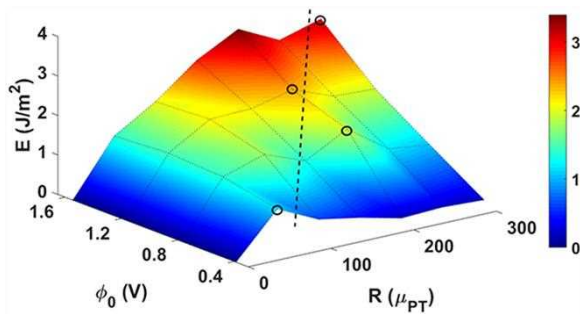

Figure 5. Demonstration of the influence of the bias voltage and bias resistance on the output energy density in PbTiO$_3$-based FEH.

where T is the time period of the strain signal; ε_{11}^0 and ε_{22}^0 denote the spontaneous strain and the transverse spontaneous strain of the specific material, respectively. As shown in equation (8), the maximum input strain is kept as 1.2 times of the spontaneous strain. The maximum input strain in PbTiO$_3$-based FEH is about six times larger than that in BaTiO$_3$-based one. Once the input strains are determined, simulations with different bias voltage and bias resistance values are carried out. The maximum bias voltage values adopted in both harvesters are based on the exact value of the electric field E_0 that is required to induce homogeneous 180° switching. In the simulations, the maximum bias electric field imposed by the bias voltage is kept as one fourth of E_0. As for the bias resistance range, they are determined by trial and error based on numerical experiments to best demonstrate their effects. The simulated results of these two harvesters are as shown in Figures 4 and 5. With a constant bias electric potential, the energy output increases first, reaches its peak and then decreases, as the bias resistance increases. This tendency is observed in both cases but is more pronounced in the BaTiO$_3$-based FEH. Furthermore, it is noticed that the energy peak is improved when the bias electric potential increases, so is the bias resistance value corresponding to the energy peak. However, it does not mean that we can increase the bias electric potential without limit to improve the energy output. The material would break

down with extreme electric fields and excessive stress. The optimized values for BaTiO$_3$-based FEH in the current parameter space are: $\varphi_0 = 0.15$ V and $R = 600\ \mu_{BT}$. The corresponding values for PbTiO$_3$ are: $\varphi_0 = 1.54$ V and $R = 300\ \mu_{PT}$. The peak output energy density for PbTiO$_3$ is approximately 20 times bigger than that for BaTiO$_3$. In conclusion, PbTiO$_3$ retains a much higher energy density, which means it can produce a much higher output electrical energy, and at the same time, a larger mechanical input strain is required. Besides, it also needs to be pointed out that the unit for the bias resistance in the results is the parameter μ instead of an SI unit. The inverse of parameter μ describes the mobility of domain walls. The rate-dependent and energy-dissipative properties of the polarization switching process in ferroelectric materials, which is important when considering FEH, are mainly characterized by parameter μ. However, most publications regarding phase-field modeling of ferroelectric materials focus only on the exact state of the material during polarization switching instead of the real time scale (Lich et al., 2015; Zhang and Bhattacharya, 2005). The parameter μ is always omitted through a non-dimensionalization technique. Further details on the influence of parameter μ will be a subject of our future publication.

Comparison of the energy-harvesting process and energy flow details

In this subsection, the details of the energy-harvesting process and energy flow in the two nanoscale FEHs with optimum bias voltage and bias resistance values are provided and carefully compared. The temporal evolution of the domain patterns in a typical energy-harvesting cycle of the BaTiO$_3$-based FEH working at the optimum condition is demonstrated in Figure 6. At the beginning of the cycle, the ferroelectric thin film is subjected to the maximum tensile strain, and all of the polarizations point in the negative x_1-direction. As the strain decreases, the tensile strain–favored horizontal polarizations become unstable and try to switch toward the vertical direction. Due to the preference imposed by the bias voltage, a domain with polarizations pointing in the negative x_2-direction nucleates at a soft-spot of the material at $t = 0.294\ T$ as shown in Figure 6(b). As the strain further decreases, the domain with compressive strain–favored vertical polarizations expands through the non-180° domain wall motion. As discussed in our previous work (Wang et al., 2017), with a sufficient large bias resistance connected to the upper electrode, which is the case in this simulation, the charge accumulated on the electrode due to the polarization switching process can not release immediately through the energy-harvesting circuit. An internal electric field pointing in the positive x_2-direction is formed.
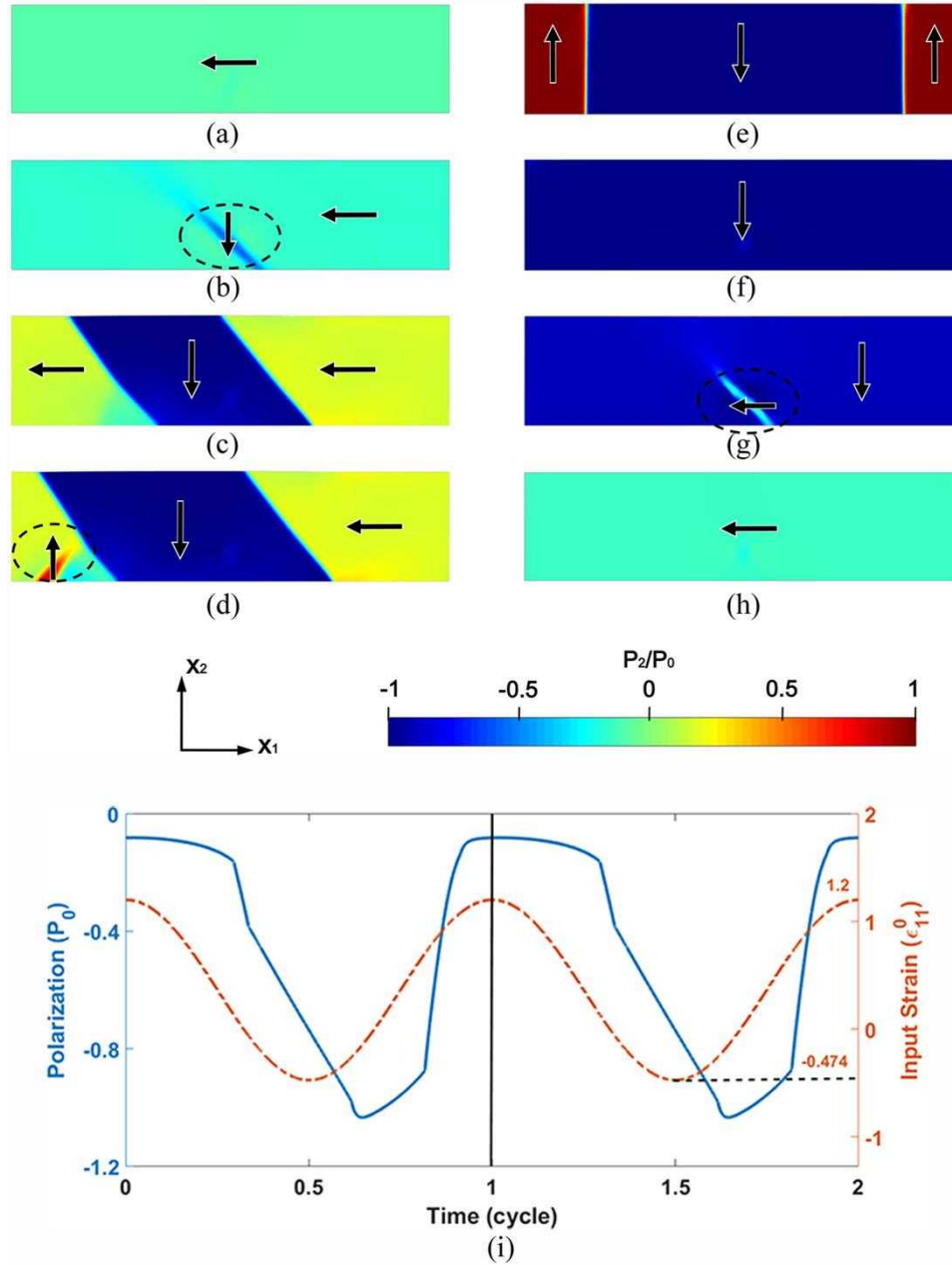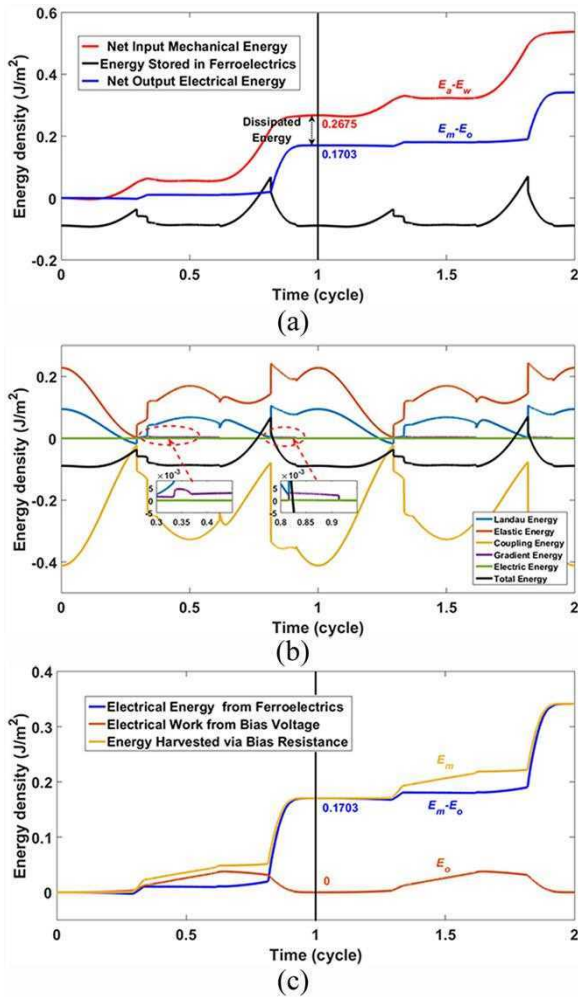
Figure 6. Demonstration of the energy-harvesting process in BaTiO$_3$-based FEH working at the optimum condition: (a) to (h) the evolution of the domain patterns in a typical energy-harvesting cycle: (a) $t = 0$, (b) $t = 0.294\ T$, (c) $t = 0.310\ T$, (d) $t = 0.334\ T$, (e) $t = 0.368\ T$, (f) $t = 0.616\ T$, (g) $t = 0.816\ T$, and (h) $t = 0.914\ T$; (i) the temporal evolution curve of the average polarization along the x_2-direction.

Therefore, a domain with polarizations preferred by the added electric field nucleates at $t = 0.334\ T$ as shown in Figure 6(d). This domain nucleation process can also release the stress concentrated near the non-180° domain wall in the proximity of the lower electrode. The domains with polarizations pointing in the positive and negative x_2-direction both grow as the strain decreases, and the entire material is occupied by the vertical polarizations at $t = 0.368\ T$. Under the influence of the bias voltage, polarizations pointing in the

positive x_2-direction switch toward the negative x_2-direction via the 180° domain wall motion, and all of the polarizations point in the negative x_2-direction at $t = 0.616\ T$ as shown in Figure 6(f). When the input cyclic strain turns tensile again and reaches a sufficient level, domains with horizontal polarizations nucleate. From the energy point of view, both types of the polarizations pointing in the negative and positive x_1-directions can be induced at this moment, but it would not affect the performance of the FEH. In this simulation,

Figure 7. Demonstration of the energy flow details in BaTiO₃-based FEH working at the optimum condition: (a) temporal evolution curves of three main energy components: net input, stored, net output; (b) temporal evolution curves of different components in the stored part; (c) temporal evolution curves of energy components involved in the energy-harvesting circuit.

a domain with polarizations pointing in the negative x_1-direction nucleates at $t = 0.816\ T$. Finally, the material is re-occupied by the horizontal polarizations and returns to its initial state, where new energy-harvesting cycles can initiate. During the energy-harvesting cycle, the average polarization along the x_2-direction varies with the input cyclic strain. The polarization variation induces an output electrical current in the energy-harvesting circuit. Thus the input mechanical energy is converted into the output electrical energy. As a reference, the temporal evolution curve of the average polarization along the x_2-direction is provided in Figure 6(i).

In addition, the energy flow details associated with the above energy-harvesting process are further demonstrated in Figure 7. Figure 7(a) shows the temporal evolution curves of the net input mechanical energy density (i.e. $E_a - E_w$), net output electrical energy

density (i.e. $E_m - E_o$), and the energy density stored in the ferroelectric transducer in two typical energy-harvesting cycles. For the BaTiO₃-based FEH, these energy densities are in the order of $10^{-1}\ \mathrm{J/m^2}$. After a complete energy-harvesting cycle, the energy stored in the ferroelectric transducer returns to its initial value and no net energy is further stored into the material, which is consistent with the fact that the domain patterns always return to their initial state at the end of the cycle. It is also noticed that the net input mechanical energy hardly decreases along the time axis, which means very few of the energy is returned to the mechanical energy source during the energy-harvesting process, that is, $E_w \approx 0$. Therefore, the input energy is either converted to the electrical energy or dissipated. From Figure 7(a), the total energy conversion efficiency η_T can be calculated as 63.66%. Considering the fact that E_w is approximately equal to zero, the effective energy-harvesting efficiency η_E can be roughly estimated by the total energy conversion efficiency η_T, which means $\eta_E \approx \eta_T = 63.66\%$. Besides, the detailed information of the different components of the stored energy in the ferroelectric transducer is demonstrated in Figure 7(b), where the temporal evolution curves of the Landau, elastic, coupling, gradient, and electrical energy are presented. Compared with other components, the gradient and electric energy are very small and their variations can hardly be noticed. At each point, where the polarization switching takes place, the coupling energy decreases rapidly, while other energy components remain constant or increase. Only the coupling energy contributes to the decrease of the total energy; therefore, the polarization switching takes place to release the coupling energy stored by the input strain. A similar phenomenon has been observed in Lich et al.'s (2015) work. Figure 7(c) demonstrates the temporal evolution curves of the energy densities involved in the energy-harvesting circuit. From the conservation law of energy, the electrical energy from the transducer added by the work from the bias voltage leads to the energy harvested by the resistance. As no electrical leakage effect is considered in this simulation, the net work done by the bias voltage in a complete energy-harvesting cycle is zero. However, it needs to be pointed out that the existence of the bias voltage is necessary, which provides a preference when the horizontal polarizations try to switch toward the vertical direction.

Figures 8 and 9 demonstrate the corresponding results of the PbTiO₃-based FEH working at the optimum condition. Compared with the energy-harvesting process of the BaTiO₃-based FEH shown in Figure 6, the main features demonstrated in Figure 8 are similar, which is reasonable, considering the fact that same physical mechanism is adopted. Cyclic input strain induces cyclic polarization switching process. However, at some moment, the detailed polarization domain
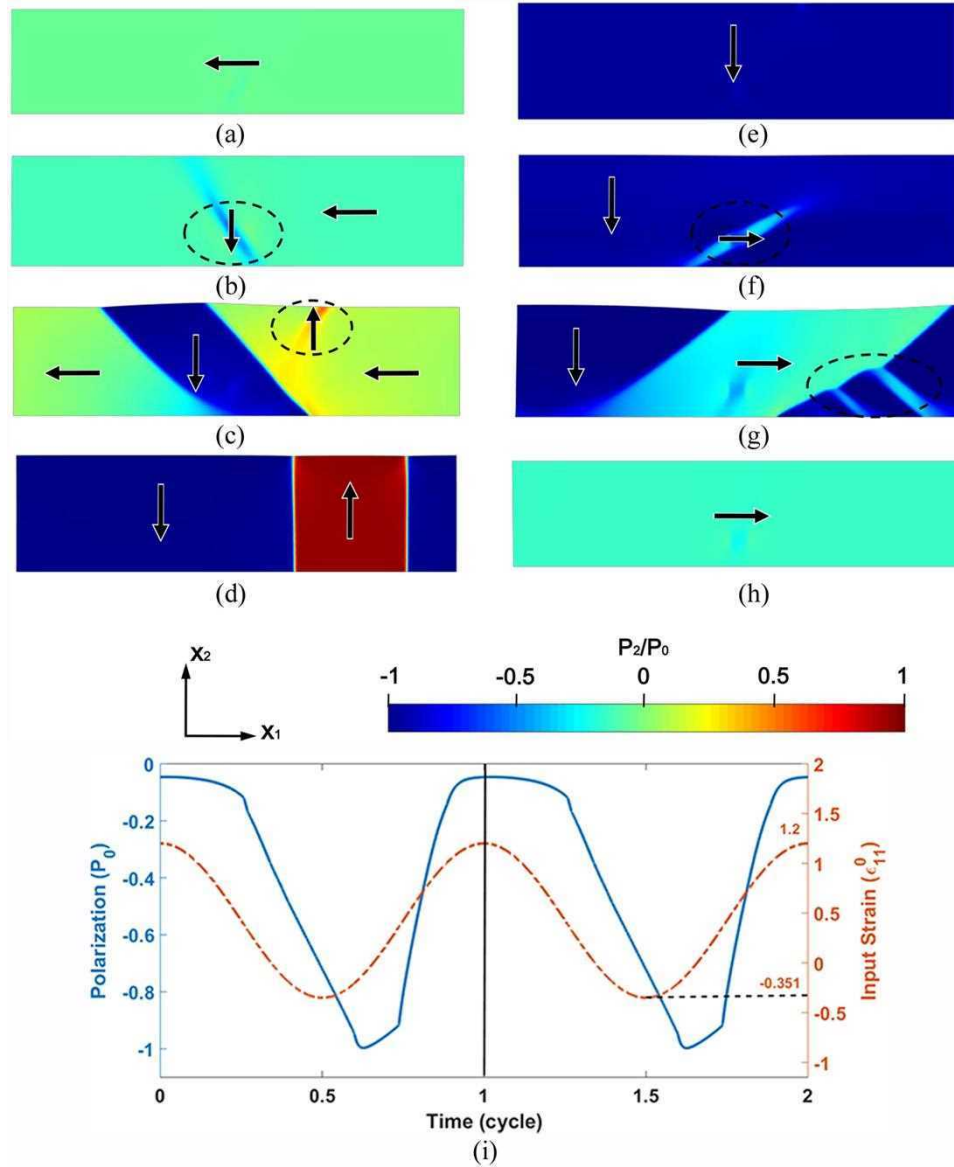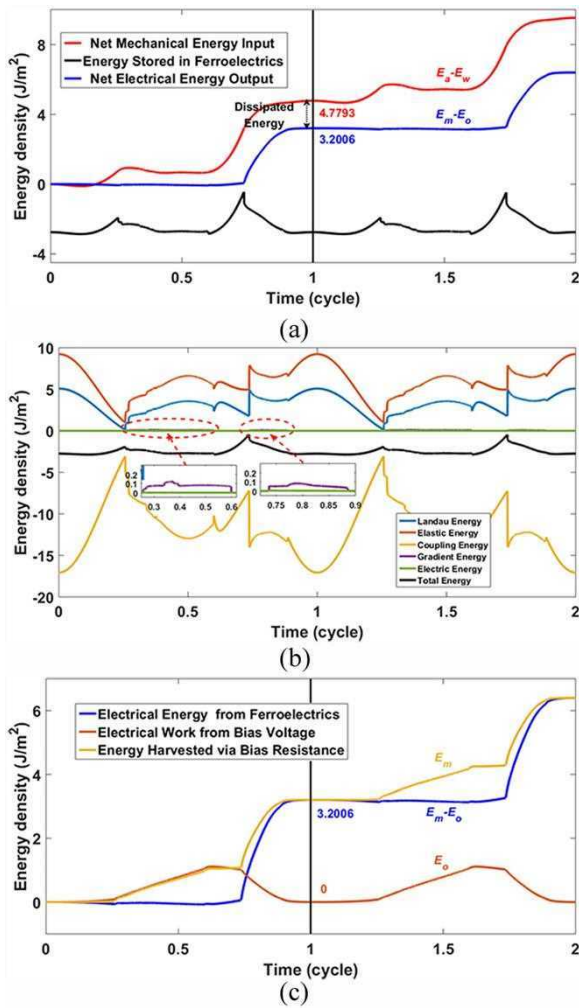
Figure 8. Demonstration of the energy-harvesting process in PbTiO$_3$-based FEH working at the optimum condition: (a) to (h) the evolution of the domain patterns in a typical energy-harvesting cycle: (a) $t = 0$, (b) $t = 0.257$ T, (c) $t = 0.269$ T, (d) $t = 0.395$ T, (e) $t = 0.600$ T, (f) $t = 0.737$ T, (g) $t = 0.781$ T, and (h) $t = 0.886$ T; (i) the temporal evolution curve of the average polarization along the x_2-direction.

patterns are more complicated in PbTiO$_3$-based FEH as shown in Figure 8(g), which can be ascribed to the much larger aspect ratio of the tetragonal phase of the PbTiO$_3$. The aspect ratio of tetragonal PbTiO$_3$ is 1.0669, while the corresponding value for BaTiO$_3$ is 1.0113. Larger aspect ratio means more complicated stress state when the polarization switching process takes place. To release the mismatched stress, detailed domain patterns are formed. On the other hand, the energy flow details of PbTiO$_3$-based FEH are demonstrated in Figure 9. The main features are also similar when compared to BaTiO$_3$. The energy densities for PbTiO$_3$ are in the order of 10^0 J/m^2, which is an order larger than that for BaTiO$_3$. In PbTiO$_3$-based FEH, to

release the coupling energy is also the main driving force for the polarization switching process; and the effective energy-harvesting efficiency η_E, and the total energy conversion efficiency η_T can be calculated as: $\eta_E \approx \eta_T = 66.97\%$.
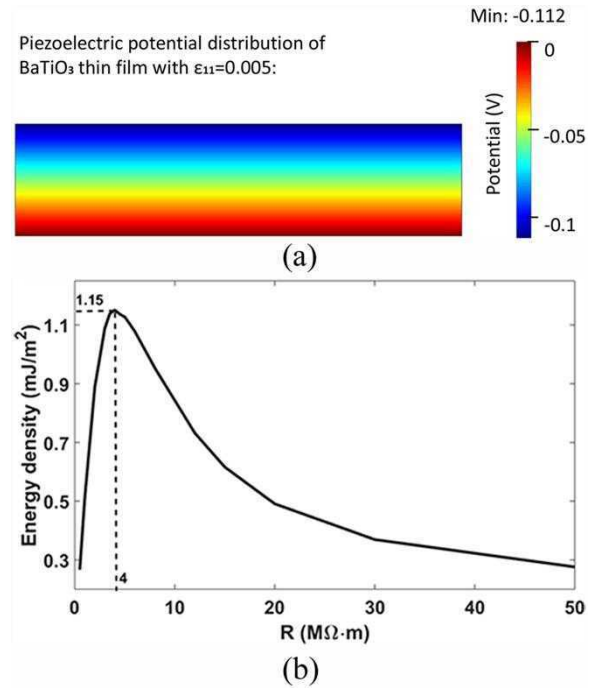
Comparison with PEH with equivalent material size

To further demonstrate the material influence and the obvious advantage associated with the newly proposed strategy, the energy-harvesting performance of a BaTiO$_3$-based PEH with equivalent material size is additionally simulated with the finite element method. Instead of the TDGL equation for ferroelectrics, the
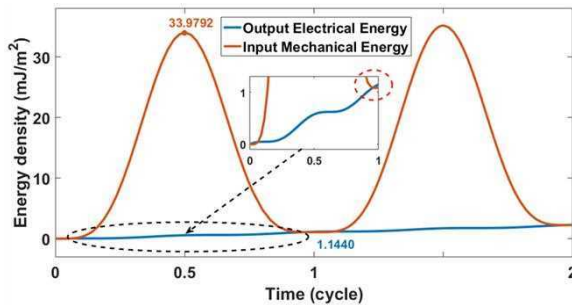
Figure 9. Demonstration of the energy flow details in PbTiO$_3$-based FEH working at the optimum condition: (a) temporal evolution curves of three main energy components: net input, stored, net output; (b) temporal evolution curves of different components in the stored part; (c) temporal evolution curves of energy components involved in the energy-harvesting circuit.

Figure 10. Demonstration of the energy-harvesting performance of the BaTiO$_3$-based PEH: (a) the piezoelectric potential distribution with $\varepsilon_{11} = 0.005$ under open-circuit condition and (b) the influence of the bias resistance on the output energy density.

linear piezoelectric relation is adopted in the simulation. The linear piezoelectric relation is plugged into the elastic and electrical governing equations to characterize the properties of the piezoelectric transducer. The boundary conditions and the element types are kept the same as those adopted in the previous phase-field simulations. The material properties are taken from Park et al.'s work (2010), where a young's modulus of 67 GPa and a piezoelectric coefficient of 78 pC/N were used. The magnitude of the input strain is kept as 0.005, which is comparable to the value assumed in Park et al.'s work (2010) and far smaller to induce the non-180° polarization switching. The piezoelectric potential distribution of the piezoelectric thin film with $\varepsilon_{11} = 0.005$ under open-circuit condition is shown in Figure 10(a), which is comparable to the result

presented in Park et al.'s work (2010) and confirms the reliability of the current simulation. Different from the FEH, no bias voltage is needed in PEH. In PEH, we only need to change the bias resistance values and optimize the performance. The influence of the bias resistance values on the output energy density is illustrated in Figure 10(b). An optimum output energy density 1.15 mJ/m^2 is obtained with the bias resistance equal to 4 MΩ m. The optimum output energy density is more than two orders smaller than that associated with the BaTiO$_3$-based FEH. Besides, the temporal evolution curves of the net input mechanical energy density and output electrical energy density are presented in Figure 11. Different from the results in FEH, the net input mechanical energy increases in the first half of the energy-harvesting cycle and decreases in the second half of the cycle, which means a large portion of the input mechanical energy flows back to the mechanical source. The effective energy-harvesting efficiency η_E in PEH suffers, which is only about 3.37%. This is a big reason why the output energy density in PEH is very small. In traditional PEH, different nonlinear effects have already been introduced to the energy-harvesting system to reduce the energy that flows back to the mechanical source. In contrast, the intrinsic nonlinear hysteretic effects in FEH can

Figure 11. Demonstration of the energy flow details in $BaTiO_3$-based PEH working at the optimum condition.

automatically limit the energy that flows back. On the other hand, if neglecting the numerical error, the net input mechanical energy all converts into the electrical energy after a complete cycle as shown in Figure 11. The total energy conversion efficiency η_T is theoretically equal to 100%.

Conclusion

The material influence in newly proposed FEH has been carefully investigated in this article. The state-of-the-art phase-field model was adopted to simulate the nonlinear hysteretic energy-harvesting process in two representative nanoscale FEHs, that is, single-crystal $BaTiO_3$- and $PbTiO_3$-based FEHs. First, different bias voltages and bias resistances were connected to these two FEHs to optimize their performance. Compared with $BaTiO_3$-based FEH, $PbTiO_3$-based FEH retains a higher energy density. The critical stain required to induce non-180° polarization switching and the output energy density in $PbTiO_3$-based FEH are both higher. The detailed comparison of the energy-harvesting process and energy flow in these two FEHs working at the optimum condition showed that the main features were very similar. However, due to the large aspect ratio of the tetragonal phase of $PbTiO_3$, the domain patterns in some specific moment were more complicated. In addition, the energy flow details showed that reducing the coupling energy was the main driving force for polarization switching in both cases. The additional finite element simulation of a $BaTiO_3$-based PEH showed that the maximum output energy density of the PEH was only 1.15 mJ/m^2, which was several orders less when compared with FEH. This small output energy can be ascribed to the fact that a large portion of the input mechanical energy flows back to the mechanical energy source, and the effective energy-harvesting efficiency η_E in PEH suffers. This study illustrated a systematic way to investigate the material influence and to optimize the device performance in FEHs, especially from the point view of energy flow.

ORCID iD

Dan Wang https://orcid.org/0000-0003-0563-8030

References

Balakrishna AR and Huber JE (2016) Nanoscale domain patterns and a concept for an energy harvester. *Smart Materials and Structures* 25(10): 104001.

Balakrishna AR, Huber JE and Landis CM (2014) Nanoactuator concepts based on ferroelectric switching. *Smart Materials and Structures* 23(8): 085016.

Chen LQ (2002) Phase-field models for microstructure evolution. *Annual Review of Materials Research* 32(1): 113–140.

Chen Y, Zhang Y, Zhang L, et al. (2017) Scalable single crystalline PMN-PT nanobelts sculpted from bulk for energy harvesting. *Nano Energy* 31: 239–246.

Daqaq MF, Masana R, Erturk A, et al. (2014) On the role of nonlinearities in vibratory energy harvesting: a critical review and discussion. *Applied Mechanics Reviews* 66(4): 040801.

Fan FR, Tian ZQ and Wang ZL (2012) Flexible triboelectric generator. *Nano Energy* 1(2): 328–334.

Invernizzi F, Dulio S, Patrini M, et al. (2016) Energy harvesting from human motion: materials and techniques. *Chemical Society Reviews* 45(20): 5455–5473.

Karami MA and Inman DJ (2012) Powering pacemakers from heartbeat vibrations using linear and nonlinear energy harvesters. *Applied Physics Letters* 100(4): 042901.

Kim S, Choi SJ, Zhao K, et al. (2016) Electrochemically driven mechanical energy harvesting. *Nature Communications* 7: 10146.

Kim SH, Haines CS, Li N, et al. (2017) Harvesting electrical energy from carbon nanotube yarn twist. *Science* 357(6353): 773–778.

Lefeuvre E, Badel A, Brenes A, et al. (2017) Power and frequency bandwidth improvement of piezoelectric energy harvesting devices using phase-shifted synchronous electric charge extraction interface circuit. *Journal of Intelligent Material Systems and Structures* 28: 2988–2995.

Liang J and Liao WH (2012) Impedance modeling and analysis for piezoelectric energy harvesting systems. *IEEE/ASME Transactions on Mechatronics* 17(6): 1145–1157.

Lich LV, Shimada T, Nagano K, et al. (2015) Anomalous toughening in nanoscale ferroelectrics with polarization vortices. *Acta Materialia* 88: 147–155.

Lich LV, Shimada T, Sepideh S, et al. (2017) Multilevel hysteresis loop engineered with ferroelectric nano-metamaterials. *Acta Materialia* 125: 202–209.

Liu J, Dai L and Baur JW (2007) Multiwalled carbon nanotubes for flow-induced voltage generation. *Journal of Applied Physics* 101(6): 064312.

Nafari A, Bowland CC and Sodano HA (2017) Ultra-long vertically aligned lead titanate nanowire arrays for energy harvesting in extreme environments. *Nano Energy* 31: 168–173.

Park KI, Xu S, Liu Y, et al. (2010) Piezoelectric BaTiO3 thin film nanogenerator on plastic substrates. *Nano Letters* 10(12): 4939–4943.

Pertsev NA, Zembilgotov AG and Tagantsev AK (1998) Effect of mechanical boundary conditions on phase diagrams of epitaxial ferroelectric thin films. *Physical Review Letters* 80(9): 1988.

Priya S and Inman DJ (eds) (2009) *Energy Harvesting Technologies*, vol. 21. New York: Springer.

Ren B, Or SW, Zhang Y, et al. (2010) Piezoelectric energy harvesting using shear mode $0.71Pb (Mg_{1/3} Nb_{2/3}) O_3$–$0.29 PbTiO_3$ single crystal cantilever. *Applied Physics Letters* 96(8): 083502.

Rezaeisaray M, El Gowini M, Sameoto D, et al. (2015) Low frequency piezoelectric energy harvesting at multi vibration mode shapes. *Sensors and Actuators A: Physical* 228: 104–111.

Roundy S, Wright PK and Rabaey J (2003) A study of low level vibrations as a power source for wireless sensor nodes. *Computer Communications* 26(11): 1131–1144.

Shaikh FK and Zeadally S (2016) Energy harvesting in wireless sensor networks: a comprehensive review. *Renewable and Sustainable Energy Reviews* 55: 1041–1054.

Sharpes N, Abdelkefi A and Priya S (2015) Two-dimensional concentrated-stress low-frequency piezoelectric vibration energy harvesters. *Applied Physics Letters* 107(9): 093901.

Shen H, Qiu J, Ji H, et al. (2010) Enhanced synchronized switch harvesting: a new energy harvesting scheme for efficient energy extraction. *Smart Materials and Structures* 19(11): 115017.

Shu YC and Bhattacharya K (2001) Domain patterns and macroscopic behaviour of ferroelectric materials. *Philosophical Magazine B* 81(12): 2021–2054.

Su Y and Landis CM (2007) Continuum thermodynamics of ferroelectric domain evolution: theory, finite element implementation, and application to domain wall pinning. *Journal of the Mechanics and Physics of Solids* 55(2): 280–305.

Wang D, Du H, Wang L, et al. (2018) A phase field approach for the fully coupled thermo-electro-mechanical dynamics of nanoscale ferroelectric actuators. *Smart Materials and Structures* 27(5): 055012.

Wang D, Wang L and Melnik R (2017) Vibration energy harvesting based on stress-induced polarization switching: a phase field approach. *Smart Materials and Structures* 26(6): 065022.

Wang ZL and Song J (2006) Piezoelectric nanogenerators based on zinc oxide nanowire arrays. *Science* 312(5771): 242–246.

Wu C, Liu R, Wang J, et al. (2017) A spring-based resonance coupling for hugely enhancing the performance of triboelectric nanogenerators for harvesting low-frequency vibration energy. *Nano Energy* 32: 287–293.

Yang Z and Zu J (2016a) Toward harvesting vibration energy from multiple directions by a nonlinear compressive-mode piezoelectric transducer. *IEEE/ASME Transactions on Mechatronics* 21(3): 1787–1791.

Yang Z and Zu J (2016b) Comparison of PZN-PT, PMN-PT single crystals and PZT ceramic for vibration energy harvesting. *Energy Conversion and Management* 122: 321–329.

Yin J, Li X, Yu J, et al. (2014) Generating electricity by moving a droplet of ionic liquid along graphene. *Nature Nanotechnology* 9(5): 378–383.

Zhang W and Bhattacharya K (2005) A computational model of ferroelectric domains. Part I: model formulation and domain switching. *Acta Materialia* 53(1): 185–198.

Zhou S, Chen W, Malakooti MH, et al. (2017) Design and modeling of a flexible longitudinal zigzag structure for enhanced vibration energy harvesting. *Journal of Intelligent Material Systems and Structures* 28(3): 367–380.

Zi Y, Guo H, Wen Z, et al. (2016) Harvesting low-frequency (<5 Hz) irregular mechanical energy: a possible killer application of triboelectric nanogenerator. *ACS Nano* 10(4): 4797–4805.